energies

Article

Compact Single-Stage Micro-Inverter with Advanced Control Schemes for Photovoltaic Systems

Yoon-Geol Choi [1], Hyeon-Seok Lee [1], Bongkoo Kang [1], Su-Chang Lee [2] and Sang-Jin Yoon [3,*]

1 Department of Electrical Engineering, Pohang University of Science and Technology, Pohang 37673, Korea; ygchoi@postech.ac.kr (Y.-G.C.); hsasdf@postech.ac.kr (H.-S.L.); bkkang@postech.ac.kr (B.K.)
2 LG Electronics Co., Ltd., Energy Business Center, Gumi 39368, Korea; suchang.lee@lge.com
3 Department of Electrical Engineering, Korea Polytechnics, Gumi 39257, Korea
* Correspondence: sjyoon@kopo.ac.kr; Tel.: +82-54-468-5248

Received: 18 March 2019; Accepted: 27 March 2019; Published: 31 March 2019

Abstract: This paper proposes a grid-connected single-stage micro-inverter with low cost, small size, and high efficiency to drive a 320 W class photovoltaic panel. This micro-inverter has a new and advanced topology that consists of an interleaved boost converter, a full-bridge converter, and a voltage doubler. Variable switching frequency and advanced burst control schemes were devised and implemented. A 320 W prototype micro-inverter was very compact and slim with 60-mm width, 310-mm length, and 30-mm height. In evaluations, the proposed micro-inverter achieved CEC weighted efficiency of 95.55%, MPPT efficiency >95% over the entire load range, and THD 2.65% at the rated power. The proposed micro-inverter is well suited for photovoltaic micro-inverter applications that require low cost, small size, high efficiency, and low noise.

Keywords: single stage micro-inverter; burst control; variable frequency control; maximum power-point tracking

1. Introduction

The photovoltaic (PV) generation is emerging as a future energy system because of its installation convenience, no-noise, infinite, and eco-friendly characteristics [1–4]. It is classified into the centralized power system and the distributed power system depending on the scale of solar power generation [5]. The centralized power system has a simple circuit structure with PV strings as the input energy source, but it has a disadvantage that the power generation is considerably lowered when some panels of the PV string are shaded. On the other hand, in the distributed power system, the optimal power extraction is possible because the maximum power point tracking (MPPT) control can be applied to each PV panel with a micro-inverter connected. So, it can minimize the loss of power generation caused by the shading effect. However, one micro-inverter is required for each PV panel, so implementation of this strategy is expensive. Therefore, many attempts have recently been made to lower the cost of micro-inverters.

In general, considering the cost, micro-inverters have been designed to use circuit architectures with a flyback converter [6–10], which provides galvanic isolation with fewer switches than other designs. Although the flyback converter has the advantage of circuit simplicity and low cost, the design must use a transformer with a high turns ratio to achieve a high voltage-conversion ratio from low dc voltage on a single PV panel. In the transformer, the high turns ratio causes a large leakage inductance which increases the stress on semiconductor switches. Moreover, due to low utilization of the transformer, this topology is most suitable for low-power applications <200 W. Recently, multi-phase interleaved technology has been applied to solar power generation from PV panels that output ≥320 W, but this technology requires large and expensive components.

This paper proposes a low-cost, slim, single-stage micro-inverter to drive a 320-W-class PV panel. The proposed micro-inverter has an interleaved structure based on the boost half-bridge (BHB) converter [11] with a cascaded voltage doubler. The interleaved BHB has an inversely-coupled inductor for the voltage step-up operation. The coupled inductor can reduce input ripple current and can be reduced in size. The voltage doubler increases the ac output voltage from the interleaved converter. Therefore, the transformer can have a lower turns ratio in the interleaved BHB than in a flyback converter and can be reduced in size. In the proposed micro-inverter, semiconductor switches achieve turn-on zero-voltage-switching (ZVS) and turn-off zero-current-switching (ZCS) by exploiting the resonance between the leakage inductance of the transformer and output capacitors of the voltage doubler, without additional components.

This paper also presents two advanced control algorithms. First, a variable switching frequency control scheme was implemented to reduce total harmonic distortion (THD) by reducing output ripple current. Then an advanced burst control scheme was implemented to improve power-conversion efficiency at light loads. By distributing output current temporally at light loads, input ripple voltage can be reduced. Therefore, the size of decoupling capacitors is reduced and MPPT efficiency is improved compared with the conventional burst control [12,13]. Section 2 describes the circuit structure and operating principles of the proposed micro-inverter, Section 3 gives the proposed control schemes, Section 4 shows experimental results using a 320-W prototype micro-inverter, and Section 5 concludes the paper.

2. Circuit Structure and Operating Principles of the Proposed Micro-inverter

The proposed micro-inverter (Figure 1) consists of an interleaved boost converter, a full-bridge converter, and a voltage doubler. The portion that is composed of the interleaved boost and full-bridge converters is based on a boost half-bridge topology. The interleaved boost converter consists of an inversely-coupled inductor L_B, four switches S_1–S_4, and a storage capacitor C_S. The full-bridge converter consists of a transformer T_1 and the same four switches S_1–S_4 as the interleaved boost converter. The voltage doubler has four switches S_5–S_8 and two capacitors C_1 and C_2.

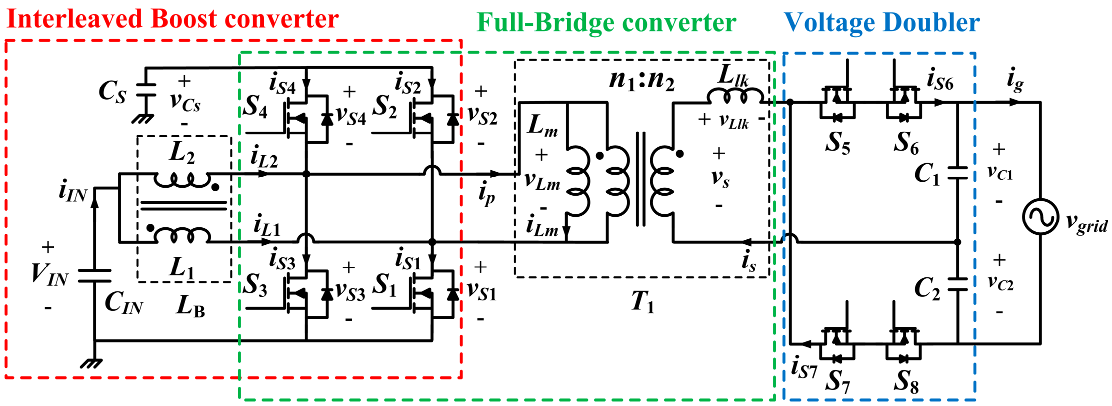

Figure 1. The circuit structure of the proposed micro-inverter.

In the proposed interleaved boost converter, two inductors L_1 and L_2 form L_B (Figure 2) by using a single magnetic core instead of two separate magnetic cores used in the conventional interleaved boost converter [14]. L_B has a turns ratio of 1:1; L_1 and L_2 each have self-inductance L. The mutual inductance M between L_1 and L_2 is represented as:

$$M = kL, \ (k < 0), \tag{1}$$

where k is the coupling coefficient. The voltage drops of L_1 and L_2 are given, respectively, by

$$v_1 = L\frac{di_1}{dt} - M\frac{di_2}{dt}, \tag{2}$$

and

$$v_2 = L\frac{di_2}{dt} - M\frac{di_1}{dt}. \tag{3}$$

Using Equations (2) and (3) and $v_m = -Md(i_1 + i_2)/dt$ yields

$$v_1 - v_m = (L + M)\frac{di_1}{dt} \tag{4}$$

and

$$v_2 - v_m = (L + M)\frac{di_2}{dt}. \tag{5}$$

S_1, the body diode of S_2, and L_1 form one boost power stage. S_3, the body diode of S_4 and L_2 form the other boost power stage. The two boost power stages form an interleaved boost converter and two outputs operate out of phase. When S_1 or S_3 is turned on, voltage v_{IN} is applied to L_1 or L_2, respectively. When S_1 or S_3 is turned off, voltage $v_{IN} - v_{Cs}$ is applied to L_1 or L_2, respectively. The energy accumulated during the on-state for each boost power stage is transferred into C_S. There are four cases of the voltage v_1 of L_1 and the voltage v_2 of L_2 depending on the states of S_1 and S_3. Using Equations (4) and (5), the equivalent inductance for each case is obtained (Table 1). $M < 0$ in Equation (1), so Table 1 demonstrates that appropriate design of the inversely coupled inductor can reduce the input ripple current of the micro-inverter [15].

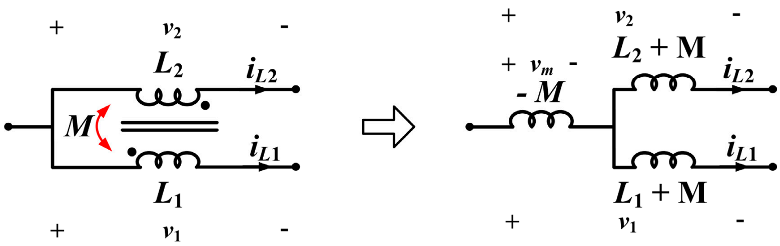

Figure 2. The equivalent circuit of the inversely coupled inductor L_B.

Table 1. Equivalent inductances in the interleaved boost converter.

Symbol	Value	Condition
L_{eq1}	$\frac{L^2-M^2}{L+DM/1-D}$	$v_1 = v_{IN}$, $v_2 = v_{IN} - v_{Cs}$
L_{eq2}	$L + M$	$v_1 = v_2 = v_{IN}$
L_{eq3}	$L + M$	$v_1 = v_2 = v_{IN} - v_{Cs}$
L_{eq4}	$\frac{L^2-M^2}{L+(1-D)M/D}$	$v_1 = v_{IN} - v_{Cs}$, $v_2 = v_{IN}$

The full-bridge converter shares four switches S_1–S_4 with the interleaved boost converter, and its input power comes from C_S. The leakage inductance L_{lk} of T_1 and capacitors C_1 and C_2 in the voltage doubler form an LC resonant circuit. The LC resonant current flows through the primary and secondary sides of T_1 with turns ratio n_1:n_2. This current causes the body diode of each switch to conduct before the turn-on gate signal is applied, thus achieving zero-voltage-switching (ZVS) for S_1–S_4.

In the voltage doubler, S_5–S_8 rectify current on the secondary side of T_1. When grid voltage is positive, both S_5 and S_8 are turned on, and both S_6 and S_7 act as diodes. When grid voltage is negative, both S_6 and S_7 are turned on, and both S_5 and S_8 act as diodes. The energy transferred to the voltage doubler through T_1 is stored in C_1 and C_2. C_1 and C_2 are connected in series, and the output voltage of the micro-inverter is the sum of the voltage v_{C1} of C_1 and the voltage v_{C2} of C_2.

In the proposed micro-inverter, variable-switching-frequency control is used, and the output voltage is a sinusoidal grid voltage. However, for simplicity, the analysis is based on the assumption that the micro-inverter generates a constant output voltage with a fixed switching frequency at a certain point in the analysis. In addition, the electrical losses of all components are ignored, and the following conditions are assumed: $2\pi\sqrt{L_{lk}(C_1+C_2)} > DT_s$ and $n^2 L_m >> L_{lk}$, where L_m is the magnetizing inductance and T_s is the switching period. The operation cycle S_1–S_4 is the same regardless of the polarity of the grid voltage, so the analysis considers only positive grid voltage.

The operating waveforms (Figure 3) of the proposed micro-inverter depend on the duty ratio D. First, operational states are analyzed for $D \leq 0.5$ (Figures 3a and 4).

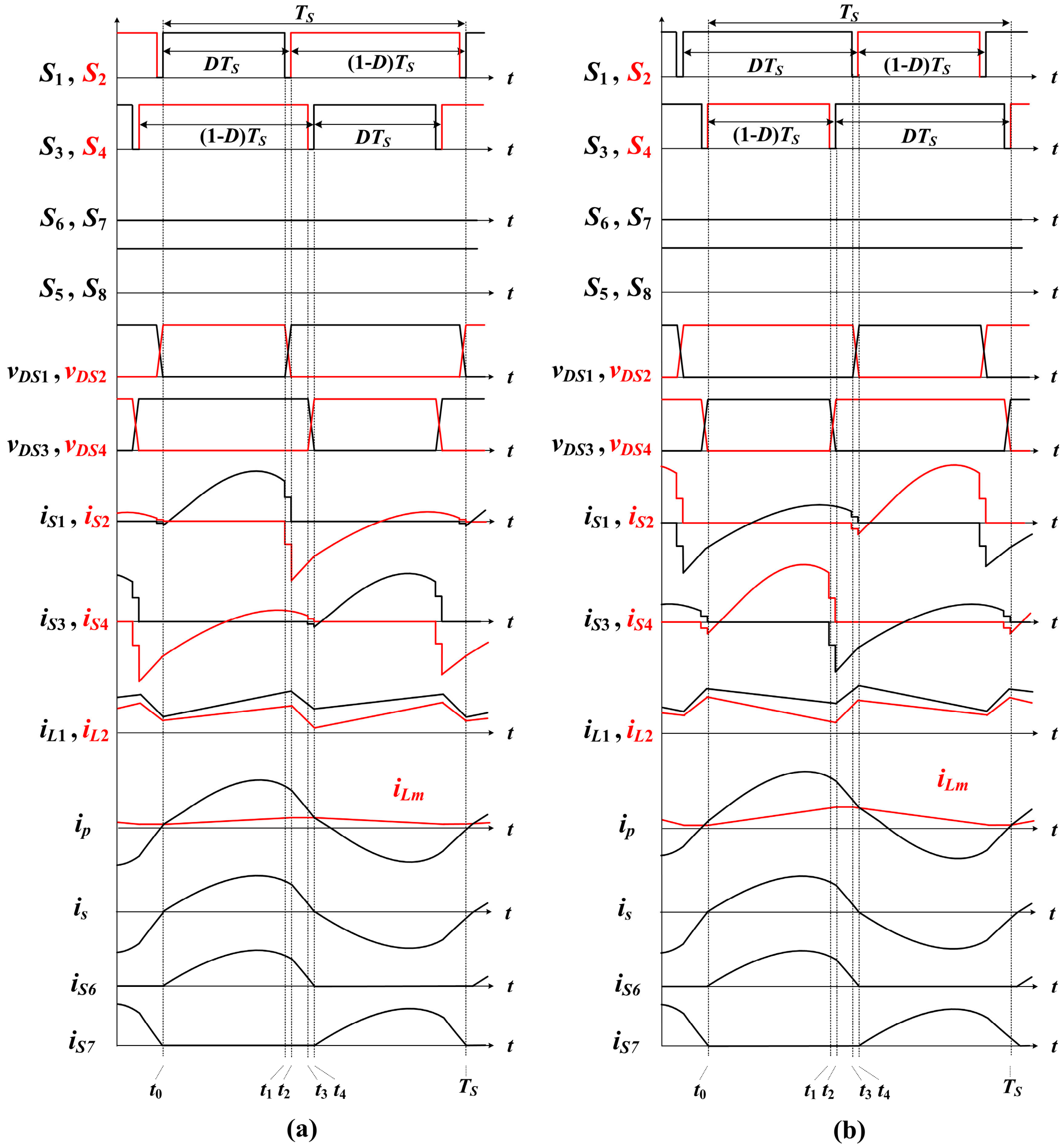

Figure 3. Operating waveforms of the proposed micro-inverter for (**a**) $D \leq 0.5$ and (**b**) $D > 0.5$.

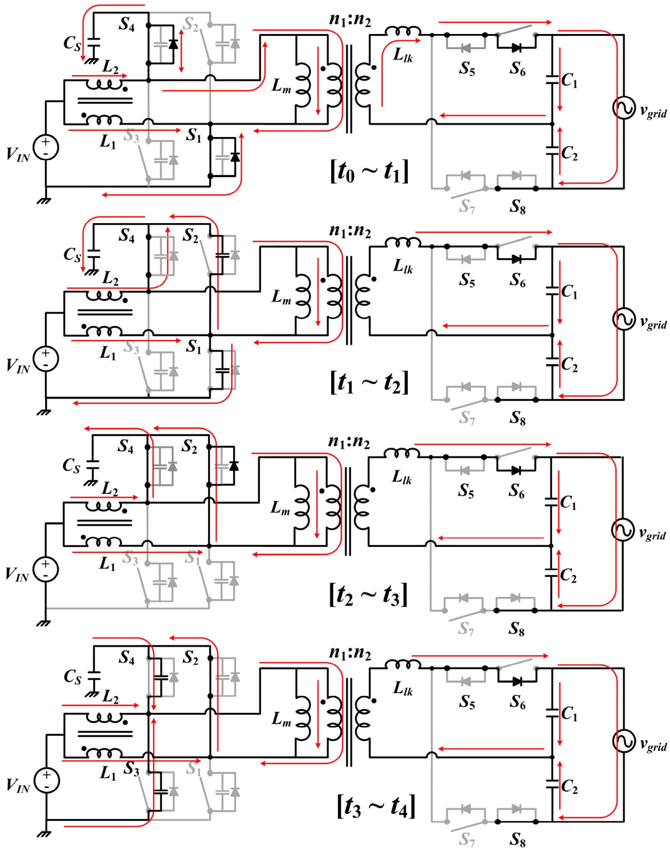

Figure 4. Operating modes when $D \leq 0.5$.

State 1 (t_0–t_1): At $t = t_0$, S_1 is turned on, $v_{DS1} = 0$, and $i_{SW1} < 0$. S_4 remains in the turn-on state, and both S_2 and S_3 remain in the turn-off state. For T_1, the voltage v_{Lm} across L_m is equal to v_{Cs}, and the secondary voltage v_s proportional to the turns ratio n_1:n_2 is generated on the secondary side of T_1. The magnetizing current i_{Lm} is increased and is given by:

$$i_{Lm}(t) = i_{Lm}(t_0) + \frac{v_{Cs}}{L_m}(t - t_0). \tag{6}$$

Resonance is generated by L_{lk} on the secondary side of T_1 and capacitors C_1 and C_2, and the state equation is given by

$$L_{lk}\frac{di_s}{dt} = nv_{Lm} - v_{C1}, \tag{7}$$

$$i_s = C_1\frac{dv_{C1}}{dt} - C_2\frac{dv_{C2}}{dt} = (C_1 + C_2)\frac{dv_{C1}}{dt}. \tag{8}$$

Using Equations (7) and (8), the secondary current i_s of T_1 is obtained as

$$i_s(t) = \frac{nv_{Lm} - v_{C1}}{Z_r}\sin[\omega_r(t - t_0)], \tag{9}$$

where

$$Z_r = \sqrt{\frac{L_{lk}}{C_1 + C_2}} \tag{10}$$

is the resonant impedance and

$$\omega_r = \frac{1}{\sqrt{L_{lk}(C_1 + C_2)}} \tag{11}$$

is the resonant angular frequency.

From Equations (6) and (9), the primary current i_p of T_1 is obtained as

$$i_p(t) = i_{Lm}(t_0) + \frac{v_{Cs}}{L_m}(t - t_0) + \frac{n^2 v_{Lm} - n v_{C1}}{Z_r} \sin[\omega_r(t - t_0)]. \tag{12}$$

From Table 1, the currents i_{L1} and i_{L2} of the coupled inductor are obtained as

$$i_{L1}(t) = i_{L1}(t_0) + \frac{v_{IN}}{L_{eq1}}(t - t_0), \quad i_{L2}(t) = i_{L2}(t_0) + \frac{v_{IN} - v_{Cs}}{L_{eq1}}(t - t_0). \tag{13}$$

State 2 (t_1–t_2): At $t = t_1$, S_1 is turned off and S_4 remains in the turn-on state. Both S_2 and S_3 remain in the turn-off state. This interval is a dead time to prevent shoot-through before S_2 is turned on. During this state, the drain-source voltage of S_1 increases from 0 V to v_{Cs} and that of S_2 decreases from v_{Cs} to 0 V by charging and discharging parallel capacitance across each switch, respectively.

State 3 (t_2–t_3): At $t = t_2$, S_2 is turned on, $v_{DS2} = 0$, and $i_{SW2} < 0$. S_4 remains in the turn-on state, and both S_1 and S_3 remain in the turn-off state. For T_1, the voltage v_{Lm} across L_m is 0 V and the voltage v_{lk} across L_{lk} is $-v_{C1}$. The amplitude of i_{Lm} remains unchanged during state 3 as:

$$i_{Lm}(t) = i_{Lm}(t_2) = i_{Lm}(t_0) + \frac{v_{Cs}}{L_m}(t_2 - t_0). \tag{14}$$

i_s begins to decrease because the energy stored in L_{lk} is transferred to C_1, and is given by

$$i_s(t) \cong i_s(t_2) - \frac{v_{C1}}{L_{lk}}(t - t_2) = \frac{n v_{Lm} - v_{C1}}{Z_r} \sin[\omega_r(t_2 - t_0)] - \frac{v_{C1}}{L_{lk}}(t - t_2). \tag{15}$$

From Equations (14) and (15), i_p is obtained as

$$i_p(t) = i_{Lm}(t_0) + \frac{v_{Cs}}{L_m}(t_2 - t_0) + \frac{n^2 v_{Lm} - n v_{C1}}{Z_r} \sin[\omega_r(t_2 - t_0)] - \frac{n v_{C1}}{L_{lk}}(t - t_2). \tag{16}$$

From Table 1, i_{L1} and i_{L2} are obtained as

$$i_{L1}(t) = i_{L1}(t_2) + \frac{v_{IN}}{L_{eq3}}(t - t_2), \quad i_{L2}(t) = i_{L2}(t_2) + \frac{v_{IN} - v_{Cs}}{L_{eq3}}(t - t_2). \tag{17}$$

State 4 (t_3–t_4): At $t = t_3$, S_4 is turned off and S_2 remains in the turn-on state. Both S_1 and S_3 remain in the turn-off state. This time interval is a dead time to prevent shoot-through before S_3 is turned on. During this state, the drain-source voltage of S_4 increases from 0 V to v_{Cs} and that of S_3 decreases from v_{Cs} to 0 V.

The proposed micro-inverter has an interleaved structure, so both the operating principle of the next half cycle for $D \leq 0.5$ and the operating principle for $D > 0.5$ are the same as the above analysis except for the switches used. Thus, further analysis for the others is not given.

The voltage gain G_v of the proposed micro-inverter is twice the product of the boost converter voltage gain and the full bridge converter voltage gain:

$$G_v = \frac{V_{grid}}{V_{IN}} = 2 \cdot \frac{1}{1 - D} \cdot 2nD = \frac{4nD}{1 - D}. \tag{18}$$

3. The Proposed Control Schemes

The main controller (Figure 5) for the proposed micro-inverter takes as analog-to-digital inputs the grid voltage v_{grid}, the grid current i_g, the input voltage V_{IN} and the input current I_{IN}. The MPPT controller is based on the perturb and observe (P&O) MPPT algorithm [16]. This controller determines the amplitude of the reference grid current I_{g_ref} by using I_{IN} and V_{IN} to maximize solar power generation. In the P&O MPPT algorithm used (Figure 6), I_{g_ref} is increased if $\Delta P_{IN} > 0$ and $\Delta V_{IN} > 0$ or if $\Delta P_{IN} < 0$ and $\Delta V_{IN} < 0$. I_{g_ref} is decreased if $\Delta P_{IN} > 0$ and $\Delta V_{IN} < 0$ or if $\Delta P_{IN} < 0$ and $\Delta V_{IN} > 0$. This process is repeated until the maximum power point (MPP) is reached, i.e., $\Delta P_{IN} = 0$.

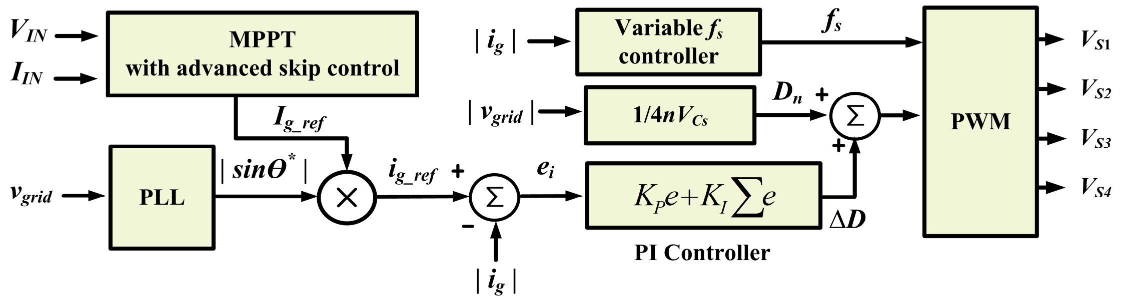

Figure 5. Block diagram of the main controller for the proposed micro-inverter.

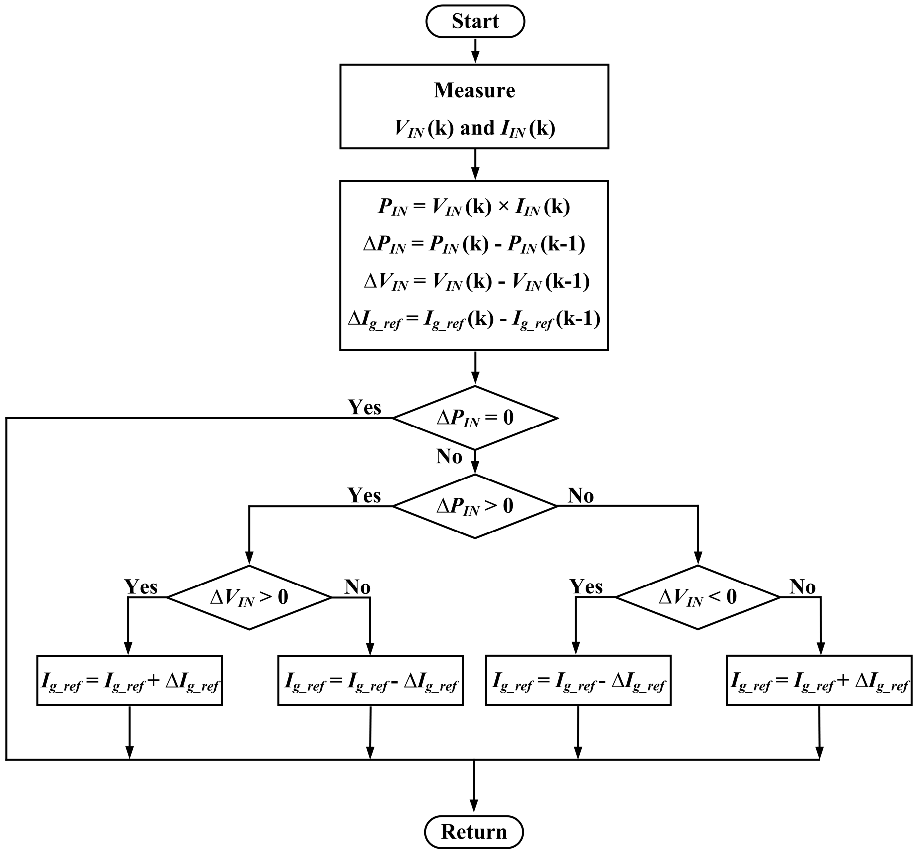

Figure 6. The perturb and observe MPPT algorithm.

The phase-locked loop (PLL) generates the phase information $|sin\,\theta^*|$ by using v_{grid}. In the PLL, virtual voltage v_{q1} is derived from v_{grid} for phase detection.

$$v_{q1}(s) = G_{PLL}(s)v_{grid}(s) = V_{grid}\left(-\frac{1}{s+\omega} + \frac{s}{s^2+\omega^2} + \frac{\omega}{s^2+\omega^2}\right), \tag{19}$$

where G_{PLL}(s) is PLL gain and V_{grid} is the amplitude of v_{grid}.

From the inverse Laplace transform of v_{q1}(s),

$$v_{q1}(t) = V_{grid}(-e^{\omega t} + \cos\omega t + \sin\omega t) \approx V_{grid}(\cos\omega t + \sin\omega t), \tag{20}$$

where ωt is the actual phase of the grid.

Using equation (20), the other virtual voltage v_{q2} is obtained as

$$v_{q2}(t) = v_{q1}(t) - v_{grid}(t) = V_{grid}\sin\omega t. \tag{21}$$

v_{grid} and v_{q2} are transformed into the synchronous reference frame as follows:

$$\begin{bmatrix} v^e{}_{grid} \\ v^e{}_{q2} \end{bmatrix} = \begin{bmatrix} \cos\theta^* & \sin\theta^* \\ -\sin\theta^* & \cos\theta^* \end{bmatrix} \begin{bmatrix} v_{grid} \\ v_{q2} \end{bmatrix}, \tag{22}$$

where θ^* is a phase output from the PLL. From Equation (22),

$$v^e{}_{grid} = V_{grid}\cos(\omega t - \theta^*) \approx V_{grid}, \tag{23}$$

$$v^e{}_{q2} = V_{grid}\sin(\omega t - \theta^*) \approx V_{grid}(\omega t - \theta^*). \tag{24}$$

The PLL generates θ^* to follow ωt through PI control inside the PLL. The reference current signal i_{g_ref} is the product of I_{g_ref} and $|\sin\theta^*|$:

$$i_{g\_ref} = I_{g\_ref}\left|\sin\theta^*\right|. \tag{25}$$

The proportional-integral (PI) controller determines the duty ratio variation ΔD by using the difference between i_{g_ref} and $|i_g|$ as follows:

$$\Delta D = K_P(i_{g\_ref} - \left|i_g\right|) + K_I\sum(i_{g\_ref} - \left|i_g\right|) \tag{26}$$

ΔD compensates for the voltage drop of L_{lk}, so that i_g follows i_{g_ref}. The nominal duty ratio

$$D_n = \frac{\left|v_{grid}\right|}{G_v} = \frac{\left|v_{grid}\right|}{4nV_{Cs}} \tag{27}$$

provides stable system dynamics for nonlinear sinusoidal waves which are difficult to control using only ΔD. The total duty ratio

$$D = D_n + \Delta D = \frac{|v_{grid}|}{4nV_{Cs}} + K_P(i_{g\_ref} - |i_g|) + K_I\sum(i_{g\_ref} - |i_g|) \tag{28}$$

where D_n is duty ratio generated by the grid voltage and ΔD is a duty ratio variation generated by the grid current. D is given to the pulse-width-modulation (PWM) controller. The PWM controller generates gate signals for switches to track the reference power.

Operating modes (Figure 7) depend on the grid current level when grid voltage is positive. When i_g is low, the proposed micro-inverter operates in discontinuous conduction mode (DCM) because i_g becomes zero before the end of the switching cycle with the period T_s. When i_g is high, continuous conduction mode (CCM) is applied.

If a fixed switching frequency is used for the operating modes, especially the DCM mode, two problems occur: (1) High grid current ripples at low grid currents increase total harmonic distortion (THD); (2) as the output power decreases, the total DCM operating time can increase over the total CCM operating time, and the power conversion efficiency of the micro-inverter can be reduced by high current stress. To solve these problems, this paper proposes two advanced control schemes: Variable-switching-frequency (VSF) control and the advanced burst (AB) control.

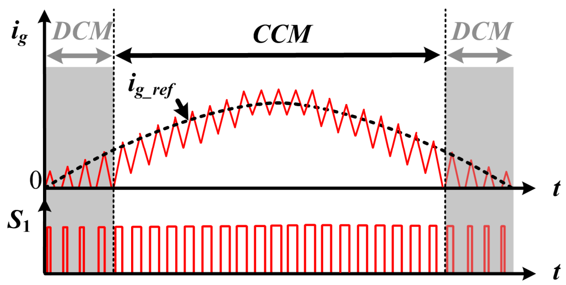

Figure 7. Operating modes depending on the grid current level during the positive grid voltage.

3.1. Variable Switching Frequency Control

During T_s, i_s of T_1 in DCM and CCM modes vary with D (Figure 8). As D decreases, the energy stored in L_{lk} decreases, so time required to demagnetize L_{lk} decreases. Therefore, the micro-inverter is operated in DCM mode. From Equations (9) and (15), the operating condition for DCM is given by

$$0 > \frac{nv_{Lm} - v_{C1}}{Z_r} \sin \omega_r DT_s - \frac{v_{C1} T_s}{2L_{lk}}(1 - 2D) \tag{29}$$

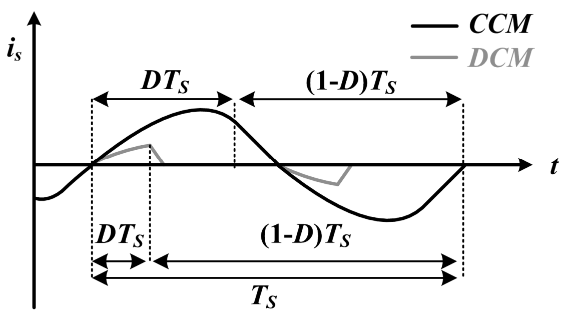

Figure 8. Secondary current i_s of the transformer T_1 depending on the operating mode.

Existing methods to optimize the DCM mode duration have drawbacks. One method is to increase the value of L_{lk}; a large L_{lk} increases the inductive energy and increases the demagnetizing time, but this solution requires a large transformer with a large number of windings. Another solution is to increase the switching frequency f_s; this approach can also increase the power density, but high f_s causes high switching loss. Thus, this paper presents VSF control, which minimizes switching loss without increasing the transformer size. VSF control varies f_s depending on the magnitude $|i_g|$ of the grid current.

Fixed-switching-frequency (FSF) control and VSF controls have distinct attributes (Figure 9). FSF control changes only D depending on v_{grid} (Figure 9a). In contrast, VSF control changes both D and f_s depending on v_{grid} (Figure 9b). When v_{grid} is near zero, the switching loss is very small because i_g is close to zero. Therefore, when VSF control is used, f_s is increased to the maximum switching frequency f_{max} and the time interval between demagnetizings of L_{lk} is reduced (Figure 9b). As v_{grid} increases, f_s is decreased to the minimum switching frequency f_{min} to reduce switching losses. f_s is given by

$$f_s = f_{\max} - (f_{\max} - f_{\max})\frac{v_{grid}}{V_{grid}} \tag{30}$$

where V_{grid} is the peak value of v_{grid}.

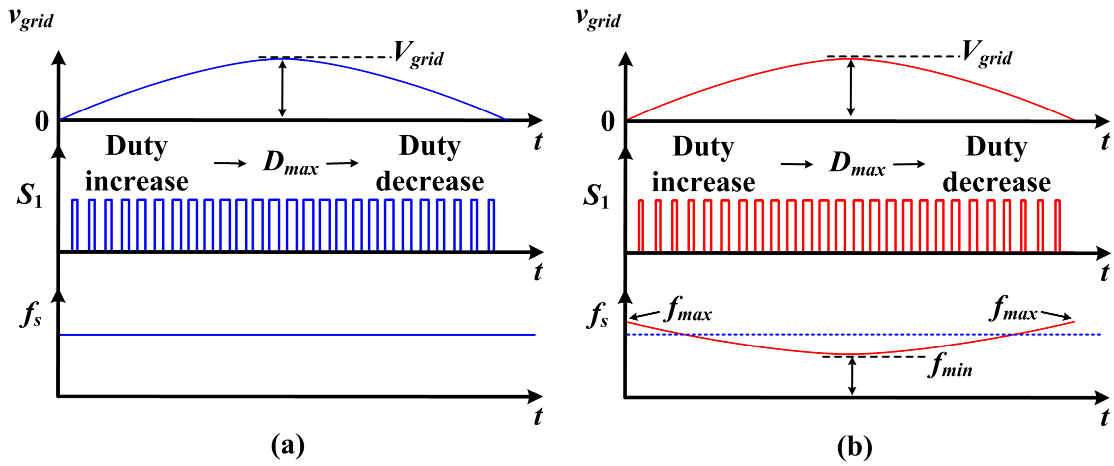

Figure 9. (**a**) Fixed and (**b**) variable switching frequency controls.

3.2. Advanced Burst Control

When solar power generation and load are very small, micro-inverters operate only intermittently to supply the desired power to the grid on an average power basis. This intermittent operation is called "burst control". For the burst control, the micro-inverter supplies i_g to the grid only during the ON state, and stops running during the OFF state. The burst control improves power-conversion efficiency by reducing the ripple of i_g and switching loss when the load is small.

In the conventional burst control scheme, positive and negative grid currents are consecutively supplied to the grid during one ON-state period (Figure 10). Then OFF-state periods follow the ON-state period. During the OFF state, no power is output, so output occurs only during the ON state, and the energy flowing out of C_{IN} is also concentrated. Therefore, the input ripple voltage ΔV_{IN} is increased, the MPPT efficiency is reduced, and additional time is required to charge the input capacitor C_{IN} for the next operation.

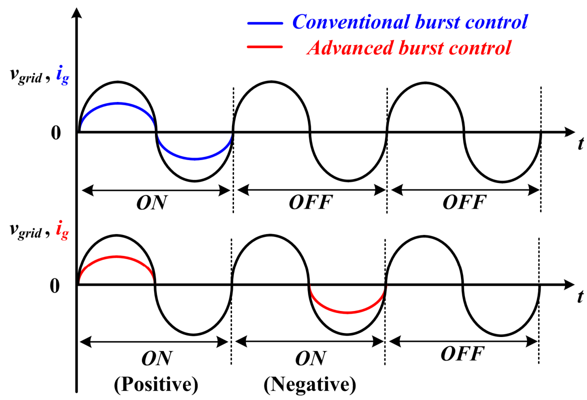

Figure 10. Conventional and advanced burst control schemes.

To further improve the performance of burst control, this paper proposes AB control, which supplies positive grid current during the first ON-state (Figure 10). The negative grid current is supplied during the ON-state that immediately follows the first ON-state period. Then, OFF-state periods follow the ON-state periods. This scheme has the effect of distributing the output current temporally compared with the conventional burst control scheme. Therefore, in the proposed micro-inverter with the advanced burst control scheme, the MPPT efficiency can be improved, and the input capacitance C_{IN} can be reduced due to the reduced ΔV_{IN}.

4. Experimental Results

The proposed grid-connected micro-inverter (Figure 11) was designed to operate at the rated power 320 W, V_{IN} = 25~52 V_{DC}, $I_{IN.max}$ = 12 A_{DC}, and f_s = 60~90 kHz. The grid voltage was 220 V_{rms}, the grid frequency was 60 Hz, and grid current supplied by the proposed micro-inverter is 0~1.45 A_{rms}. The proposed micro-inverter was implemented using the circuit parameters given in Table 2. The microcontroller used was a MN103DF35 (PANASONIC). For the PI controller in the main controller, K_P and K_I were experimentally optimized and set to 9.5 and 200, respectively. The sampling frequency for analog signals is 20 kHz, and the resolution of the analog-to-digital converter is 12 bits. The turns ratio of L_B is 10:10 and that of T_1 is 6:19. The resonant frequency f_r = 35.5 kHz from L_{lk} = 100 µH and C_1 = C_2 = 100 nF. The MOSFET package of S_1–S_4 is PG-TDSON-8 and that of S_5–S_8 is D^2PAK. Capacitors C_s, C_1 and C_2 are MPP-film type. The fabricated micro-inverter was compact and slim with 60-mm width, 310-mm length, and 30-mm height.

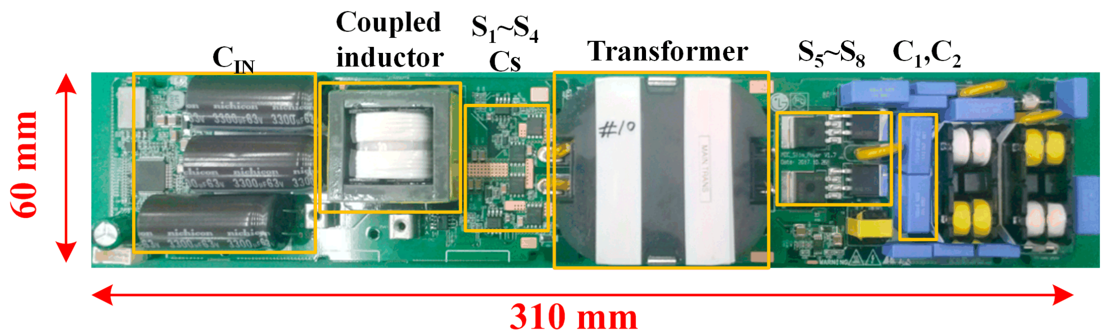

Figure 11. Photograph of the proposed micro-inverter.

Table 2. Hardware specifications and circuit parameters.

Unit Type	Symbol	Value	Note
Micro Inverter	P_o	320 W	Output power
	C_{IN}	9900 µF	Input capacitor
	L_1, L_2	190 µH	Self inductance (k = −0.947)
	S_1–S_4	BCS035N10NS5	MOSFET (V_{DS} = 100 V, I_D = 100 A)
	C_s	60 µF	Storage capacitor
	L_m	600 µH	Magnetizing inductance
	L_{lk}	100 µH	Leakage inductance
	S_5–S_8	IPB65R150	MOSFET (V_{DS} = 650 V, I_D = 22.4 A)
	C_1, C_2	100 nF	Doubler capacitors
	f_s	60~90 kHz	Switching frequency
	v_{grid}	220 V_{rms}/60 Hz	Grid voltage
	i_g	~1.45 A_{rms}/60 Hz	Grid current
	V_{IN}	25~52 V_{DC}	Operating voltage range
	$I_{IN.max}$	12 A_{DC}	Max input current
PV module	V_{PV}	40.9 V	Open circuit voltage
	V_{MP}	34 V	MPP voltage
	I_{PV}	10.05 A	Short circuit current
	I_{MP}	9.38 A	MPP current

Instead of an actual PV module, the photovoltaic simulator ETS600X14CPVF TerraSAS from AMETEK was used as an input source. The solar cell *I-V* characteristic curve for the experiment was based on that of the NeON®2 PV module from LG electronics.

Gate-source and drain-source voltages were obtained for S_1 and S_2 at $D \leq 0.5$ (Figure 12a) and at $D > 0.5$ (Figure 12b) at V_{IN} = 34 V and v_{grid} = 220 V_{rms} /60 Hz. The drain-source voltage v_{DS1} of S_1 drops to 0 V before the gate signal v_{S1} is applied, so S_1 turns on with ZVS. S_2 is complementary to S_1

and achieves a ZVS turn-on. The operation of S_3 and S_4 is out of phase with that of S_1 and S_2, so S_3 and S_4 can also achieve the ZVS turn-on.

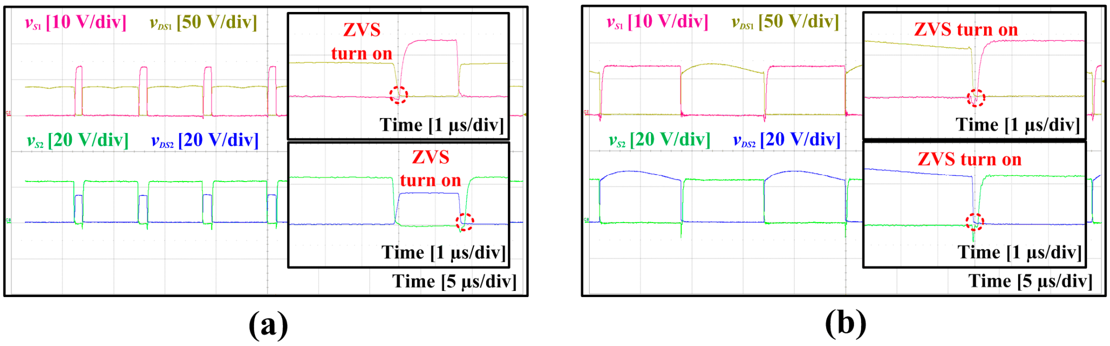

Figure 12. Gate-source and drain-source voltages of S_1 and S_3 for (**a**) $D \leq 0.5$ and (**b**) $D > 0.5$.

Waveforms (Figure 13) were obtained for v_{grid} and i_g at V_{IN} = 34 V and v_{grid} = 220V$_{\mathrm{rms}}$ / 60 Hz for output power P_o = 320 W and 64 W. To maximize efficiency, the proposed micro-inverter operates in normal mode at $P_o \geq$ 110 W and in AB control mode at $P_o <$ 110 W. The boundary of the output power at which the proposed micro-inverter switches from the normal mode to AB control mode and vice versa is selected to be in a range where the peak value of i_g does not exceed the rated grid current.

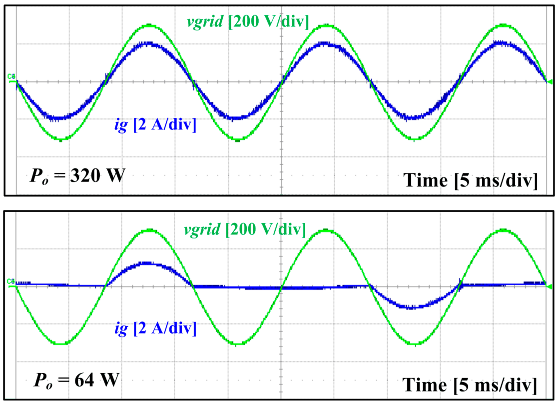

Figure 13. Grid voltage and current waveforms.

Waveforms were obtained for the fixed-frequency (Figure 14a) and the variable-switching-frequency (Figure 14b) controls. Gate signals of S_1 and S_3, i_g and v_{grid} were measured at V_{IN} = 34 V, v_{grid} = 220 V$_{\mathrm{rms}}$ / 60 Hz, and output power P_o = 320 W. When fixed-switching frequency control was used, i_g was distorted near zero-crossing, and THD was increased to 5.79%. In contrast, when variable switching frequency control was used, the distortion of i_g was improved near zero-crossing, and THD was reduced to 2.65%, which is below the requirement for distributed power. The switching frequency f_s decreased as i_g increased, so switching loss was also reduced.

ΔV_{IN} is higher when conventional burst control is used (Figure 15a) than when AB control is used (Figure 15b), because AB control reduces the energy supplied by C_{IN} during one ON-state period. At V_{IN} = 34 V, v_{grid} = 220 V$_{\mathrm{rms}}$ / 60 Hz, and P_o = 32 W, ΔV_{IN} was 4.2 V when conventional burst control was used, but 2.4 V when AB control was used.

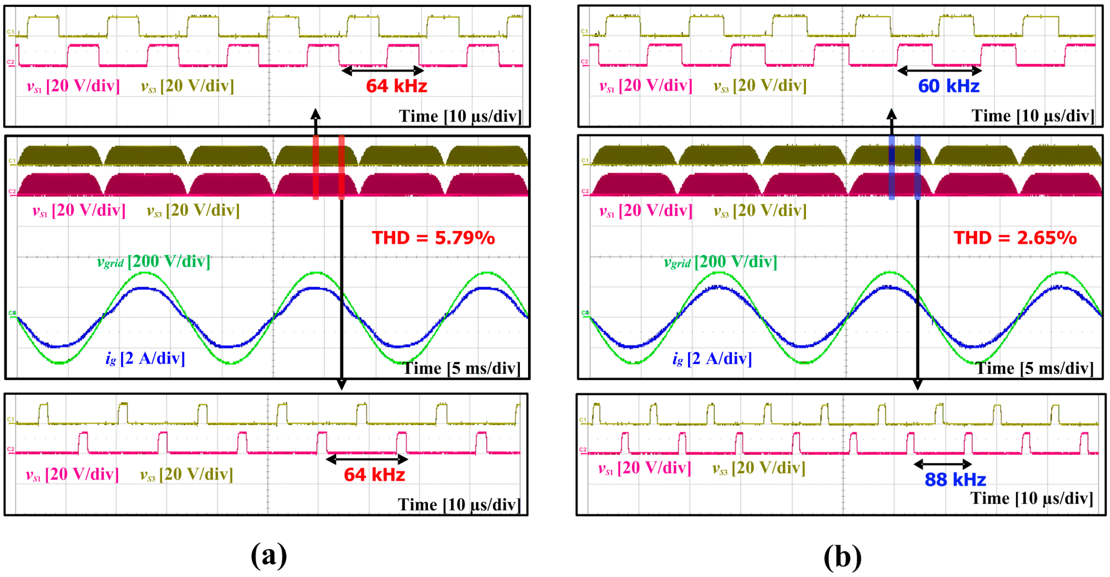

Figure 14. Gate signals of S_1 and S_3, grid voltage and grid current in (**a**) the fixed and (**b**) the variable switching frequency controls.

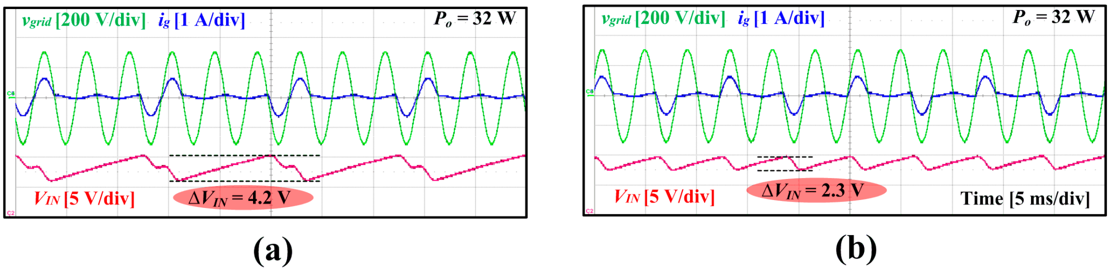

Figure 15. Input ripple voltage in (**a**) the conventional and (**b**) the advanced burst controls.

The MPPT efficiency of the proposed micro-inverter was measured (Figure 16) in the range of irradiance from 50 W/m^2 (P_o = 16 W)–1000 W/m^2 (P_o = 320 W). In the proposed control scheme, for P_o < 110 W (burst mode), the MPPT efficiency was kept >95% because ΔV_{IN} and ΔI_{g_ref} are reduced. However, in the conventional control scheme, the MPPT efficiency was reduced to ~88% because fluctuation of I_{g_ref} increased. During burst mode, the maximum MPPT efficiency was >99% for the proposed control scheme but <97.5% for the conventional control scheme.

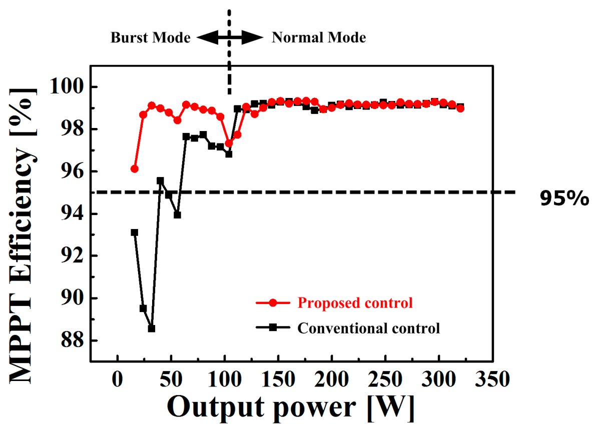

Figure 16. MPPT efficiency depending on control methods.

In a micro-inverter, one of the most important factors is the power conversion efficiency η_e for 50~75% load under actual solar irradiation. Therefore, the California Energy Commission (CEC) weighted efficiency to represent this fact has been widely used to measure the performance of micro-inverters. The power conversion efficiency η_e (Figure 17) was measured for the proposed micro-inverter; the result indicate that the CEC weighted efficiency [17,18] is 95.55%, in which η_e(10%) = 91.71%, η_e(20%) = 94.42%, η_e(30%) = 95.28%, η_e(50%) = 96.06%, η_e(75%) = 95.8%, and η_e(100%) = 95.72%. The maximum η_e is 96.06% for P_o = 160 W.

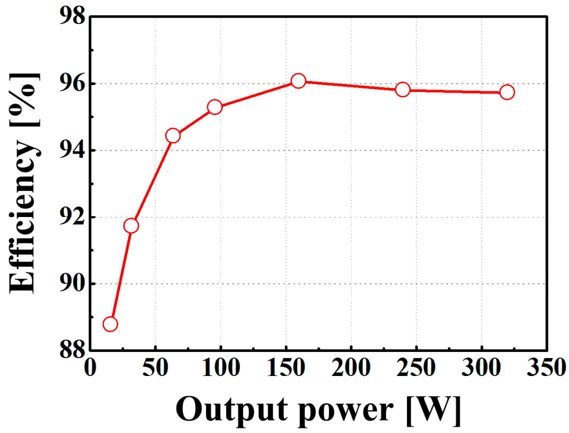

Figure 17. Power conversion efficiency η_e measured at V_{IN} = 34 V and v_{grid} = 220 V_{rms}/60 Hz.

5. Conclusions

A compact single-stage micro-inverter with advanced control schemes for PV systems is described. The proposed micro-inverter achieved a high voltage-conversion ratio and high efficiency by using a new topology that consists of an interleaved boost converter, a full-bridge converter, and a voltage doubler. The leakage inductance of the transformer and the capacitors of the voltage doubler ensure ZVS condition without any additional components. A variable-switching-frequency control scheme is applied to the micro-inverter to decrease THD by reducing the grid ripple current. An advanced burst-control scheme increases MPPT efficiency with smaller input ripple voltage than the conventional burst control causes. A fabricated 320-W prototype micro-inverter was very compact and slim with 60-mm width, 310-mm length, and 30-mm height. It achieved CEC weighted efficiency of 95.55%, MPPT efficiency > 95% over the entire load rage, and THD 2.65% at V_{IN} = 34 V, v_{grid} = 220 V_{rms}/60 Hz, and P_o = 320 W. These results show that the proposed micro-inverter is well suited for PV micro-inverter applications that require low cost, small and slim size, high efficiency, and low noise.

Author Contributions: Y.-G.C. conceived the main idea for the proposed micro-inverter and performed overall analysis and experiment with H.-S.L., B.K. led the project and gave technical advice. S.-C.L. contributed to determining circuit parameters and fabricating a prototype. S.-J.Y. contributed to analyzing the experimental results and writing the manuscript with Y.-G.C.

Acknowledgments: This research was supported by the Ministry of Science and ICT (MSIT), Korea, under the "ICT Consilience Creative Program" (IITP-2018-2011-1-00783) supervised by Institute for Information & communications Technology Promotion (IITP).

Conflicts of Interest: The authors have no conflict of interest.

References

1. Lee, S.-W.; Cho, B.-H. Master–Slave Based Hierarchical Control for a Small Power DC-Distributed Microgrid System with a Storage Device. *Energies* **2016**, *9*, 880. [CrossRef]
2. Han, H.; Luo, C.; Hou, X.; Su, M.; Yuan, W.; Liu, Z.; Guerrero, J.M. A Cost-Effective Decentralized Control for AC-Stacked Photovoltaic Inverters. *Energies* **2018**, *11*, 2262. [CrossRef]

3. Huang, L.; Qiu, D.; Xie, F.; Chen, Y.; Zhang, B. Modeling and Stability Analysis of a Single-Phase Two-Stage Grid-Connected Photovoltaic System. *Energies* **2017**, *10*, 2176. [CrossRef]
4. Jeong, H.-G.; Kim, G.-S.; Lee, K.-B. Second-Order Harmonic Reduction Technique for Photovoltaic Power Conditioning Systems Using a Proportional-Resonant Controller. *Energies* **2013**, *6*, 79–96. [CrossRef]
5. Blaabjerg, F.; Chen, Z.; Kjaer, S.B. Power electronics as efficient interface in dispersed power generation system. *IEEE Trans. Power Electron.* **2004**, *19*, 1184–1194. [CrossRef]
6. Nanakos, A.C.; Christidis, G.C.; Tatakis, E.C. Weighted efficiency optimization of flyback microinverter under improved boundary conduction mode (i-BCM). *IEEE Trans. Power Electron.* **2015**, *30*, 5548–5564. [CrossRef]
7. Rezaei, M.A.; Lee, K.J.; Huang, A.Q. A high-efficiency flyback micro-inverter with a new adaptive snubber for photovoltaic applications. *IEEE Trans. Power Electron.* **2016**, *31*, 318–327. [CrossRef]
8. Chen, Y.; Liao, C. A PV micro-inverter with PV current decoupling strategy. *IEEE Trans. Power Electron.* **2017**, *32*, 6544–6557.
9. Voglitsis, D.; Papanikolaou, N.; Kyritsis, A.C. Incorporation of harmonic injection in an interleaved flyback inverter for the implementation of an active anti-islanding technique. *IEEE Trans. Power Electron.* **2017**, *32*, 8526–8543. [CrossRef]
10. Milad, K.; Ehsan, A.; Hosein, F. Micro-inverter based on single-ended primary-inductance converter topology with an active clamp power decoupling. *IET Power Electron.* **2018**, *11*, 73–81.
11. Jafari, M.; Malekjamshidi, Z.; Li, L.; Zhu, J.G. Performance analysis of full bridge, boost half bridge and half bridge topologies for application in phase shift converters. In Proceedings of the International Conference on Electrical Machines and Systems, Busan, Korea, 26–29 October 2013; pp. 1589–1594.
12. Zhao, Z.; Wu, K.-H.; Lai, J.-S.; Yu, W. Utility grid impact with high penetration PV micro-inverters operating under burst mode using simplified simulation model. In Proceedings of the Energy Conversion Congress and Exposition (ECCE), Phoenix, AZ, USA, 17–22 September 2011; pp. 3928–3932.
13. Du, Y.; Xiao, W.; Hu, Y.; Lu, D.D.-C. Control approach to achieve burst mode operation with DC-link voltage protection in single-phase two-stage PV inverters. In Proceedings of the Energy Conversion Congress and Exposition (ECCE), Pittsburgh, PA, USA, 14–18 September 2014; pp. 47–52.
14. Thiyagarajan, A.; Praveen Kumar, S.G.; Nandini, A. Analysis and comparison of conventional and interleaved DC/DC boost converter. In Proceedings of the Second International Conference on Current Trends In Engineering and Technology—ICCTET 2014, Coimbatore, India, 8 July 2014; pp. 198–205.
15. Wong, P.; Wu, Q.; Xu, P.; Bo, Y.; Lee, F.C. Investigating coupling inductors in the interleaving QSW VRM. In Proceedings of the APEC 2000, Fifteenth Annual IEEE Applied Power Electronics Conference and Exposition (Cat. No.00CH37058), New Orleans, LA, USA, 6–10 February 2000; pp. 973–978.
16. Ahmed, A.S.; Abdullah, B.A.; Abdelaal, W.G.A. Mppt algorithms: Performance and evaluation. In Proceedings of the 11th International Conference on Computer Engineering & Systems (ICCES), Cairo, Egypt, 20–21 December 2016; pp. 461–467.
17. *Building Energy Efficiency Standards*; California Energy Commission: Sacramento, CA, USA, 2019.
18. Zhang, L.; Sun, K.; Hu, H.; Xing, Y. A system-level control strategy of photovoltaic grid-tied generation systems for European efficiency enhancement. *IEEE Trans. Power Electron.* **2014**, *29*, 3445–3453. [CrossRef]